

Journal of
***Mechanics of
Materials and Structures***

A MULTISCALE MODEL OF THE ORGAN OF CORTI

Charles R. Steele, Jacques Boutet de Monvel and Sunil Puria

Volume 4, N° 4

April 2009

A MULTISCALE MODEL OF THE ORGAN OF CORTI

CHARLES R. STEELE, JACQUES BOUTET DE MONVEL AND SUNIL PURIA

The organ of Corti is the sensory epithelium in the cochlea of the inner ear. It is modeled as a shell-of-revolution structure with continuous and discrete components. Our recent work has been on the inclusion of the viscous fluid. Measurements from various laboratories provide the opportunity to refocus on the elastic properties. The current detailed model for the organ of Corti is reasonably consistent with diverse measurements. Most components have little stiffness in the propagation direction. However, the isotropic stiffness of the pillar heads is found to offer an explanation for the difference in point load and pressure measurements. The individual rows of inner hair cell stereocilia with tip links and the Hensen stripe are included, since these details are important for the determination of the neural excitation. The results for low frequency show a phase of tip link tension similar to auditory nerve measurements. The nonlinearity of fluid in the small gaps is considered. A result is that as amplitude increases, because of the near contact with the Hensen stripe, the excitation changes polarity, similar to the peak-splitting neural behavior sometimes observed.

1. Introduction

The cochlea of the inner ear is a transducer, as described in many sources, such as [Geisler 1998].¹ The input is the sound, which causes air pressure to act on the tympanic membrane after propagating through the outer ear. Generally, the middle ear alleviates the impedance mismatch between the external air and the fluid of the cochlea. With a change in area from the eardrum to the stapes, which is the last bone of the middle ear, the amplitude of input pressure is increased without significantly affecting the time pattern. The output of the cochlea is electrical, consisting of the firings of the 30,000 individual nerve fibers that comprise the auditory nerve in humans. These signals are conducted along the auditory pathway in the brain, ending in the auditory cortex, where perception takes place.

The remarkable feature is that the nerve fibers from the cochlea are sharply tuned to frequency, so the cochlea can be considered as providing an on-line Fourier analysis of the input time signal. The cochlea establishes many basic features of hearing, such as frequency discrimination and the interaction of multiple input tones. The accuracy and ranges of frequency and amplitude of this transducer are better than man-made devices by orders of magnitude. Therefore there are both the interesting scientific question of how such a device works and the related medical question of what can be done about malfunction.

The cochlea is frequently approximated by a *box model*, in which the coiling is neglected and the geometry of the input region, containing the input piston (the stapes) and a relief window (the round window), is grossly simplified. The box is long (diameter around 1 mm and length 30 mm in humans)

Keywords: model, cochlea, Corti, pillars, tip link, point load.

This work was supported by Grant RGP0051 from the Human Frontier Science Program and by NIH Grant 5R01DC7910.

¹Many web pages deal with the cochlea. For the purposes of this article one of the most helpful is the page maintained by F. Mammano and R. Nobili of the Venetian Institute of Molecular Medicine, <http://147.162.36.50/cochlea/index.htm>.

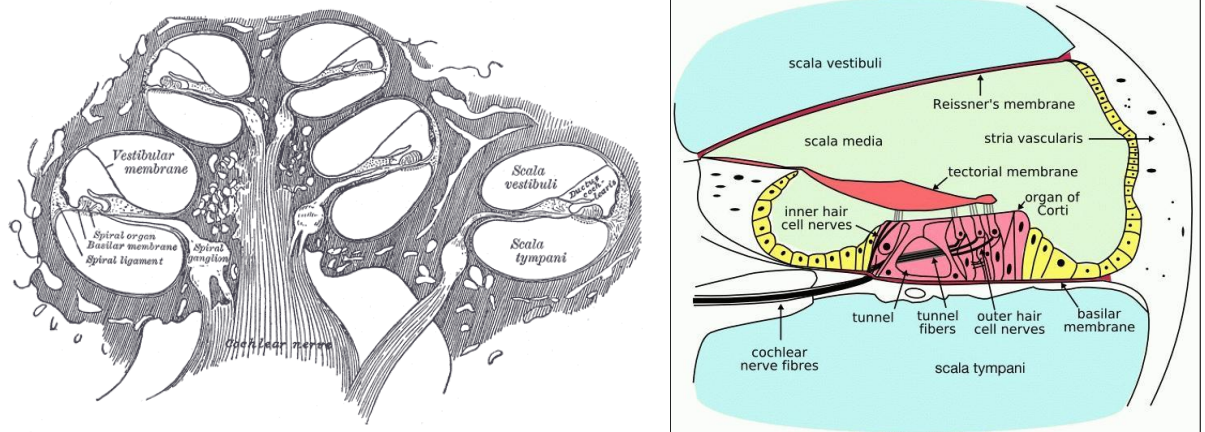
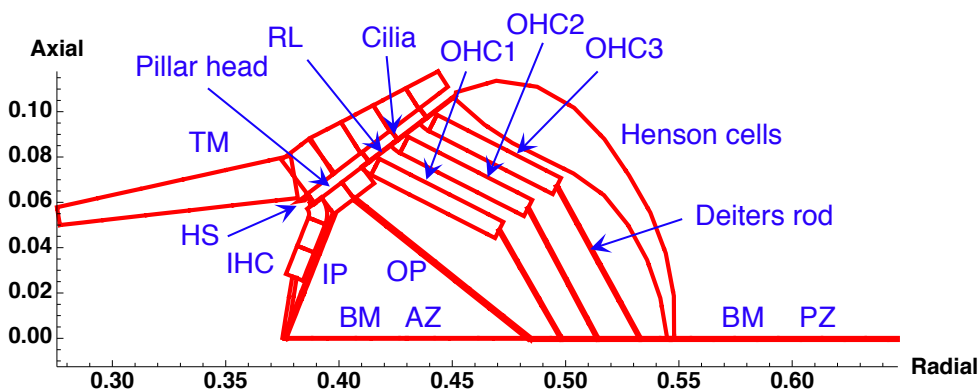


Figure 1. The cochlea is a long tapering tube that spirals around a bundle of nerve fibers. These fibers connect all along the tube to sensor cells located in a wall that partitions the tube lengthwise into two regions, the scala vestibuli and the scala tympani. (As seen on the right there is a third chamber, the scala media, but for our purposes it and the scala vestibuli can be regarded as one.) From [Gray 1918, Fig. 928] and [Wikipedia 2004].

and is filled with fluid with mechanical properties close to water. A partition divides the box along the length into two regions: the scala vestibuli (SV) connected to the input stapes, and the scala tympani (ST) connected to the round window. The partition is similar to a rigid plate with an elastic strip in the middle, the basilar membrane (BM). The stiffness of the elastic region is relatively high near the stapes (the base) and low at the far end (the apex of the coiled cochlea). The magnitude of stiffness is such that for frequencies in the auditory range, there is a significant interaction between the fluid and the elasticity of the basilar membrane. The result is a traveling, fluid-elastic wave that reaches maximum amplitude at a particular distance from the stapes and then decreases rapidly. The decrease is caused by the dissipation due to fluid viscosity when the wavelength is short. Because of the gradient in stiffness of the basilar membrane, there is a correspondence between the location of the maximum and frequency of excitation. High frequency creates a maximum near the base and low frequency a maximum near the apex.

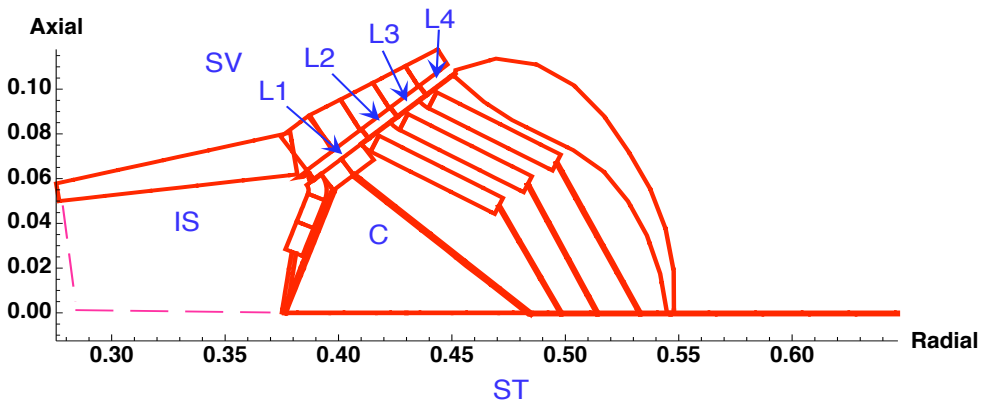
Along the elastic portion of the partition is a sensory epithelium called the organ of Corti (OC), shown schematically in Figures 2 and 3. This is an elaborate elastic structure containing receptor cells, consisting of one row of inner hair cells (IHC) and three rows of outer hair cells (OHC). In the present work, we focus on the elastic and fluid-elastic aspects of this organ. The basic question is how the motion of the basilar membrane, indicated by the simple box model, is transmitted to the inner hair cells, into which the majority of the neural fibers project.

The auditory nerve threshold is close to the basilar membrane response, as shown in the chinchilla cochlea [Narayan et al. 1998]. However the complex arrangement of the OC makes it likely that the actual excitation of the stereocilia of the inner hair cells does not merely follow the motion of the basilar membrane. Hence there is interest in developing more detailed simulations of this organ [Steele and Puria 2005; Cai and Chadwick 2002; Andoh and Wada 2003].



BM = basilar membrane	Flexible portion of the partition separating the two chambers of the cochlea (scala vestibuli and scala tympani).
IHC = inner hair cell	Primary receptors, since connected to the majority of the neural fibers.
OHC = outer hair cell	Three rows, designated OHC1, OHC2, and OHC3. Much less innervation than the inner hair cells. Walls are piezoelectric, which enable them to play significant role in feedback enhancement of the vibration.
IP = inner pillar	Stiffening rod near the IHC, consisting of a bundle of microtubules.
OP = outer pillar cilia (or stereocilia)	Stiffening rod near OHC1. Together the IP and OP are called the arches of Corti. The “hairs” on each hair cell. Tip links connect the rows of stereocilia. When in tension, ion channels open and the hair cell depolarizes. This provides the basic transduction of mechanical force to neural discharge.
AZ = arcuate zone	Thin portion of the BM, between the IP and OP. The AZ, IP and OP form a stiff triangular structure.
PZ = pectinate zone	Thick portion of the basilar membrane between the OP and the support on the right. Consists of a double layer of radial collagen fibers, with little longitudinal elastic stiffness.
TM = tectorial membrane	Thick membrane overlying the organ of Corti. Gelatinous with low elastic modulus and somewhat orthotropic.
HS = Hensen’s stripe	Strip of material that is attached to the TM, and seems to form a pocket for the tips of the stereocilia of the IHC.
RL = reticular lamina	Thin conical shell containing heads of all hair cells, through which stereocilia protrude.
Hensen cells	Soft cells attached to the RL and BM, forming the boundary of the organ of Corti on the right.
Deiters rod	Bundle of microtubules connecting base of each OHC to the BM.

Figure 2. Elastic elements in shell of revolution model for the organ of Corti in the apical region of the guinea pig cochlea. The radial and axial distances are in mm.



SV = scala vestibuli	Fluid region on which input sound pressure acts through the stapes. (In our model, the scala media and scala vestibuli are merged.)
ST = scala tympani	Fluid region to which relief window (round window) is connected.
IS = inner sulcus	Fluid region, bounded by the TM above and the IHC to the right, with stiff walls on the partition below and to the left (not shown).
C = cortilymph	Fluid filling the organ of Corti, surrounding the OHC, OP, and Deiters rods.
L1 = layer 1	Fluid beneath the TM and between the stereocilia of the IHC and the OHC1. The successive subepithelial membrane fluid regions are designated as L2, L3, and L4.

Figure 3. Fluid regions in model for the apical region of the guinea pig cochlea.

Our earlier investigation [Steele and Puria 2005] was motivated by the measurements of the inner hair cell response by Cheatham and Dallos [1999] in the upper turns of the guinea pig cochlea and the auditory nerve and basilar membrane responses in the base of the chinchilla [Ruggero et al. 2000]. The inner hair cells at the apex behave as might be expected, with a maximum excitation when the BM is between maximum displacement and velocity toward scala vestibuli. However, the neural recordings at the base indicate excitation with velocity toward scala tympani. It was found in [Steele and Puria 2005] that the phase of inner hair cell excitation, related to the tension in the tip link of the tallest stereocilium of the inner hair cell, can be anything, particularly depending on the elastic properties of the overlying tectorial membrane. However, at the guinea pig base, with tectorial membrane elastic properties given by the measurements in [Shoelson et al. 2004; Freeman et al. 2003], the excitation occurs for basilar membrane displacement and velocity toward scala tympani, consistent with measurements in [Ruggero et al. 2000], while at the apex, the excitation is for basilar membrane displacement and velocity toward scala vestibuli, consistent with measurements in that region [Cheatham and Dallos 1999].

The present effort continues [Steele and Puria 2005] with a focus on a thorough reevaluation of the recent experimental results on geometry and stiffness to improve the model. Secondly, the nonlinear solution for the full OC model is developed. The nonlinearities considered are: (1) the buckling of supporting structures (the inner and outer pillar cells and the Dieters rods); (2) the nonlinear flow of fluid in the confined region under the overlying tectorial membrane.

2. Box model without organ of Corti

It is remarkable that the OC may be stripped off, leaving only the BM as an orthotropic, sandwich plate dividing the two fluid regions, for a model that does rather well for describing the fluid-elastic waves [Yoon et al. 2006]. There is actually a third fluid region containing endolymph on the side of the OC. However, this is merged with the scala vestibuli for the usual two-chambered box model. Even with such simplifications, the computation including the three-dimensional viscous fluid by direct methods is daunting, requiring 5–20 hours on a high-speed parallel computer for the time integration of a few cycles of response [Givelberg and Bunn 2003]. Instead we advocate the use of the WKB asymptotic wave analysis method in the frequency domain, with which the computation time is around one second per frequency on a desktop computer. Our application of this method to the three-dimensional analysis of the cochlea is an extension of previous work in two dimensions [Ranke 1950]. The WKB method is well known for treatment of ordinary differential equations [Olver 1974] when solutions vary “rapidly” while the coefficients vary “slowly”. Carlini [1817] apparently used this approximation for the first time. The extension to the cochlea is possible because the wavelength of the traveling wave is generally small in comparison with the distance over which the stiffness of the BM varies significantly. Thus the local wave number can be calculated from the three-dimensional fluid equations coupled with the plate equations at a given cross section, assuming that the properties are constant.

Validation. The calculated results [Steele and Taber 1979] compare well with experimental measurements in a 6-times life-sized box model of the human cochlea [Helle 1974]. This experimental model is important because Helle measured all the properties, including the BM viscoelastic property and the viscosity of the fluid, as well as all the geometry. The objection to the use of Helle’s physical model as a “gold standard” for confirming a basic cochlear calculation is the size. To correspond to the human cochlea, scaling of the properties of stiffness and viscosity must be done, and it is difficult to have all parameters scaled properly. Several laboratories are developing life-sized models. In our effort [Wittbrodt et al. 2006] there is reasonably good agreement between the three-dimensional WKB solution and the direct measurements for the amplitude and phase of the traveling wave on the BM. Further validation comes from the excellent agreement between the calculations from the box model with three-dimensional viscous fluid, without adjustment of parameters, [Yoon et al. 2006] and the *in vivo* measurements of pressure in the fluid [Olson 1998]. Therefore the use of asymptotic methods seems justified for extension to a more detailed model with OC included.

3. Extension to detailed organ of Corti

Despite the success of the simple box model, the OC has an important role that has yet to be explained properly. We saw in Figure 2 the significant elastic elements of the OC, while Figure 3 highlighted the fluid regions. Both figures represent a radial cross section of a nearly axisymmetric configuration, with the axis running vertically on the left. Therefore we consider the OC as a shell-of-revolution structure consisting of discrete and orthotropic elastic elements. There are no air pockets in the cochlea, so the regions not taken by elastic tissue are filled with fluid that has the mechanical properties of water.

3.1. Analysis. In the finite element approach [Cai and Chadwick 2002; Andoh and Wada 2003], a fine mesh is used for the entire cross section including the fluid and tissue. Our approach [Steele 1999] is

to extend the WKB approach for the simple box model by considering a limited number of degrees of freedom for each fluid region. The simplest is to consider the one-dimensional approximation for each of the interior regions. With this the pressure is assumed to be constant in the cross section of each fluid region. Thus for the fluid regions in Figures 2 and 3, the problem reduces to just eight degrees of freedom, one for the volume displacement in the circumferential direction of each fluid region. Since the present results are obtained as a continuation of [Steele and Puria 2005], the details of the equations will not be repeated here.

The basic relations are as follows. The change in cross-sectional area for the fluid regions is given by the vector \mathbf{D}_w that is related to the vector of pressures acting on the walls of the regions \mathbf{F}_w by an elastic compliance matrix \mathbf{E} :

$$\mathbf{D}_w = \mathbf{E} \cdot \mathbf{F}_w. \quad (1)$$

The compliance matrix is symmetric with positive diagonal terms. The individual term E_{ij} is the cross-sectional area change of region i due to a unit pressure on region j . The fluid flow between the regions in the cross section is described by the relation of the vector of fluid area changes \mathbf{D}_f and the pressures with a permeability matrix \mathbf{C} :

$$\dot{\mathbf{D}}_f = -\mathbf{C} \cdot \mathbf{F}_w, \quad (2)$$

in which the dot represents the time derivative. The permeability matrix is also symmetric with positive diagonal terms. The longitudinal (circumferential) displacement of fluid in the regions is given by the vector \mathbf{Q} . The continuity condition provides the relation

$$\dot{\mathbf{Q}}_{,x} = \dot{\mathbf{D}}_f - \dot{\mathbf{D}}_w = -(\mathbf{C} \cdot \mathbf{F}_w + \mathbf{E} \cdot \dot{\mathbf{F}}_w), \quad (3)$$

in which x is the longitudinal arc length (the distance along the cochlea from the stapes). Finally the equation for motion of the fluid in the longitudinal direction is:

$$(\mathbf{A} \cdot \mathbf{F})_{,x} = -(\rho \ddot{\mathbf{Q}} + \mathbf{B} \cdot \dot{\mathbf{Q}}), \quad (4)$$

in which \mathbf{F} is the vector of averaged pressures, \mathbf{A} is the diagonal matrix of areas, \mathbf{B} is the diagonal matrix of viscous resistance, and ρ is the density of the fluid. Equations (3) and (4) are just an extension of the familiar one-dimensional model, if the averaged pressure is assumed to be the same as the pressure on the wall:

$$\mathbf{F} \approx \mathbf{F}_w. \quad (5)$$

Generally, this is a poor approximation, particularly in the region of maximum amplitude, so the three-dimensional fluid behavior must be considered to relate the averaged and wall pressures, as described in the preceding section. In the present work, however, the focus is on the low frequency response for which the wavelength is long, (5) is valid, and the longitudinal displacement of fluid is small, that is, $\mathbf{Q} = 0$. Therefore (3) reduces to

$$\mathbf{C} \cdot \mathbf{F} + \mathbf{E} \cdot \dot{\mathbf{F}} = 0 \quad (6)$$

which describes the low frequency, viscous motion of the cochlear cross section in Figures 2 and 3.

4. Static response of organ of Corti

The static elastic response (1) is crucial. Our approach, continued from [Steele 1999; Steele and Puria 2005], is to use the computer program Fast4, which is specifically developed for the efficient treatment of structures consisting of shells of revolution [Steele and Shad 1995].

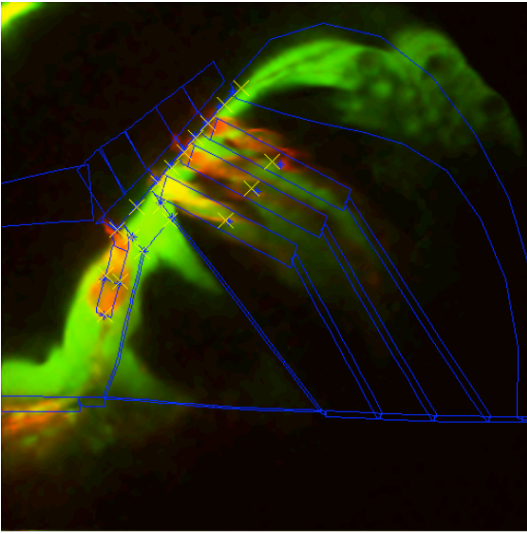
With this program, adjacent components may have elastic moduli and/or dimensions differing by orders of magnitude. The cochlea is just such a multiscale problem, with the bone of the partition having dimensions on the millimeter scale, the hair cells and supporting cells on the micrometer scale, and the tip links connecting stereocilia having thickness on the nanometer scale. The elastic moduli of the components vary from the gelatinous TM around 10 kPa to the bone of the partition and walls at 20 GPa. The table for input [Steele 1999] has some 80 geometric and material properties. Much of the geometry can be obtained from a high quality micrograph of the cross section. With a knowledge of the protein fibers, an estimate can be made for the effective stretching and bending stiffness of a particular element. However, uncertainty remains, for example, in the volume fraction of protein in a particular element and in the stiffness of ground substance. Following are the current considerations for refinement and verification.

4.1. Consistency with the anatomy. Much detail for the anatomy at the guinea pig apex is available, including average values and standard deviations of the dimensions of elements from 35 cochleas [Kelly 1989]. Ulfendahl and colleagues provide good cross sections for different distances from the stapes. The lengths and densities of microtubules in pillar cells, Deiters rod and the phalangeal process in guinea pigs at different distances from the base are also available [Zetes et al. 2004]. We assume that the distribution of the BM collagen fibers in cat [Cabezudo 1978] holds for guinea pig.

A substantial advance is provided by a new confocal microscopic technique [Fridberger et al. 2002]. The preparation is an excised guinea pig cochlea. However, the observation is through a hole in the bone at the apex, so no damage is done to the OC and the support structure on both edges of the BM. A penetration through the fluid and tissue provides good detail of the stereocilia, hair cells and pillars, but only a small portion of the BM.

A difficulty in interpreting the optical results is that the image plane is not the radial section, but at some angle of rotation about a radial line and an angle about the cochlear axis. Therefore an optimization program was developed [Boutet 2007] that we briefly outline. The first step is to determine the unknown optical angles with the knowledge of the geometry [Kelly 1989]. Figure 4 shows the Fast4 representation in blue lines added to the optical section. The elements are rectangular in the radial plane, but appear trapezoidal in the optical section. So the shell model agrees reasonably well with the actual geometry. The next step is to obtain the proper stiffness for the elastic components to obtain a best fit with the measured displacements. The starting point is component stiffness from the consideration of various other measurements.

4.2. Consistency with stiffness measurements. Information on the static stiffness of the components of the OC in guinea pig is available. This includes the static point load stiffness at points across the BM in the guinea pig base [Miller 1985] and the stiffness of microtubules and cross bridging in the pillar cells [Tolomeo and Holley 1997]. With an advance in atomic force microscopy, the impedance at points across the RL, with BM constrained and TM removed, for the frequency range 0.5 to 40 kHz has been



Click to play
or use URL in caption

Figure 4. Optical image of OC at the apex of the guinea pig cochlea [Fridberger et al. 2002] with Fast4 shell model superposed (blue lines). This shows the configuration with the maximum downward pressure, which causes a buckling of the IP. In the animation (which can be found at <http://pjm.math.berkeley.edu/jomms/2009/4-4/jomms-v4-n4-x10-corti.avi>) the blue and yellow X symbols represent fixed points that initially coincide, so the maximum discrepancy can be seen in OHC3. The animation shows both the upward and downward displacement due to steps in the static pressure.

obtained [Scherer and Gummer 2004]. The impedance provides the static stiffness and the effective thickness of the RL [Steele et al. 2005]. The isolated TM has been measured in guinea pigs [Abnet and Freeman 2000; Shoelson et al. 2004], and apparently has an effective Young's modulus of 10–30 kPa. A most thorough measurement of the stiffness of stereocilia is also available [Langer et al. 2001]. The OHC attract considerable attention because they have the unusual property of *electromotility*, that is, the wall has piezoelectric properties. Thus a change in the intracellular electrical potential, in addition to causing excitation of neurons connected to the base, cause a change in the length of the cell. This most likely pumps energy into the motion of the BM in the normal function of the cochlea. The elastic and piezoelectric coefficients are determined from a summary of isolated cell measurements [Spector et al. 1999]. With the usual composite structure analysis, the properties of the components of the OC are found that generally satisfy the condition of consistency with the microstructure, the geometry, and the static stiffness measurement.

4.3. Consistency with the quasistatic motion of the OC. An example of the calculation for the deformation due to a static pressure load acting on the BM is shown in Figure 5. Note the opening of the fluid region L1 near the stereocilia of the IHC. This does not occur in previous simplified models of the OC. The close view of the stereocilia is in Figure 6. It appears that the tips of the tall stereocilia are close to the HS, as shown by the dashed lines for the undeformed configuration. The fluid flow in this restricted region is of considerable importance in the dynamic response.

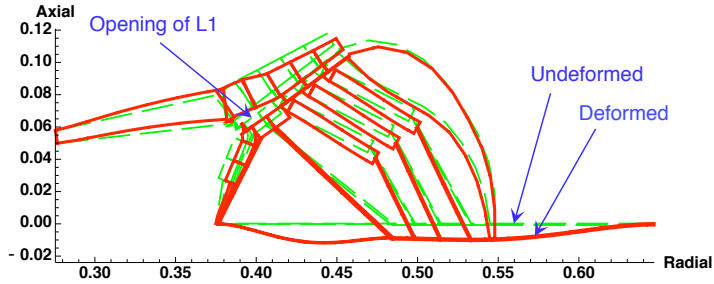


Figure 5. Deformation due to static pressure loading of the BM toward the ST. The dashed and solid lines show the undeformed and deformed configurations, respectively. Note the opening of the fluid region L1.

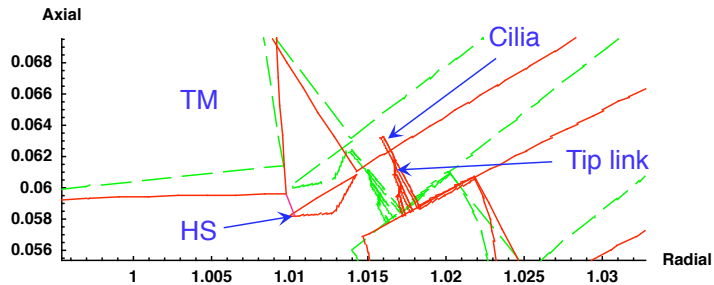


Figure 6. Close view of the stereocilia on the inner hair cell. The Hensen stripe (HS) is the triangle attached to the TM above. The green dashed lines show the undeformed configuration, with the tip of the tallest stereocilium near the HS. The red solid lines show the deformed configuration, greatly amplified. The radial and axial distances are in mm. Tip links connect the three rows of stereocilia.

Much more detail is provided by Fridberger et al. [2002], who subject the OC to quasistatic steps in pressure difference between SV and ST. The values at every pixel are recorded. One example is in Figure 7, which shows the displacement of a point at the middle of OHC3 for the steps in loading. There is a pronounced difference in the displacement magnitude and direction for loading in the two directions. This strong nonlinearity we attribute to a buckling of the IP. The model calculations indicate that the IP is

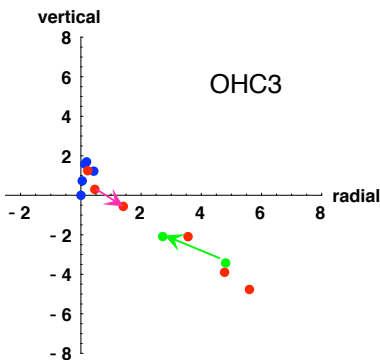


Figure 7. Measurement of displacement at the center of OHC3 for the guinea pig apex with steps in static pressure [Fridberger et al. 2002]. Dimensions are in μm . The blue points are for the initial loading steps in the upward direction. The red points show first unloading and then steps in downward loading. Finally the green points are for unloading. We attribute the severe nonlinearity to a buckling of the IP for downward loading.

subjected to compressive loading for the downward pressure loading large enough to cause buckling. The amplitude of displacement is several μm , which is much larger than the normal range for hearing. Thus from the current estimates, it appears unlikely that this effect is of physiological significance. However, this nonlinear behavior provides some confirmation that standard elastic structural analysis is applicable for such tissue.

The nearly linear behavior in Figure 7 for downward loading indicates that the buckling transition occurs in the first $1\ \mu\text{m}$ of displacement. Consequently, a reduced elastic modulus for the IP provides a simulation of the postbuckled behavior of the structure.

4.4. Tuning stiffness values with optimization. A complete optimization program has been developed for adjusting the stiffness values for the individual components of the OC, to achieve a best fit to the measured displacement at a number of points [Boutet 2007]. Figure 4 shows the agreement between the calculation and the measurements at the maximum downward displacement. A subset of points is marked by the blue and yellow X 's. For the initial configuration of zero pressure, these coincide. The maximum discrepancy at this maximum downward displacement can be seen to be at OHC3. The animation of Figure 4 for the steps of loading in both directions shows that the calculation and measurement nearly coincide.

An important point is that the beginning values of stiffness are those from the estimates for the microstructure and the various static measurements, discussed in the preceding section. The final values from the optimization are generally within an order of magnitude of the original values, which is considered to be reasonable.

4.5. Consistency between point and pressure loading. Additional information on the elastic structure of the OC is revealed from the displacement at points under a probe, as first measured by von Békésy [1960]. Furthermore, Cooper [2000] observes that the radial profile of displacement of the BM is ubiquitous for frequencies below, at, and above that producing maximum displacement in several animals, including gerbil and guinea pig. Certainly for the low frequencies, the loading of the BM should be just pressure. So we consider a simple beam model for the BM as shown in Figure 8 with point loading and pressure loading. The beam consists of the thinner AZ and the thicker PZ. In addition, the possible support of the outer pillar in Figures 2 and 3 is represented by the spring with spring constant k .

Homer et al. [2004] optimize such a beam model, without the spring ($k = 0$), to produce Cooper's radial profile of displacement under a pressure loading. They find that clamping of the right edge and hinging of the left edge produces the best results.

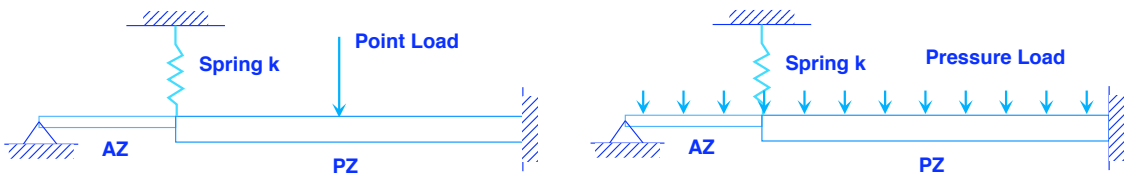


Figure 8. Simple beam model for BM. As in [Homer et al. 2004] the beam is clamped on the right end and simply-supported on the left end. However, we add a spring attachment to simulate the outer pillar and include the different thicknesses in the AZ and PZ. The experimental results are for point load (left) and pressure loading (right).

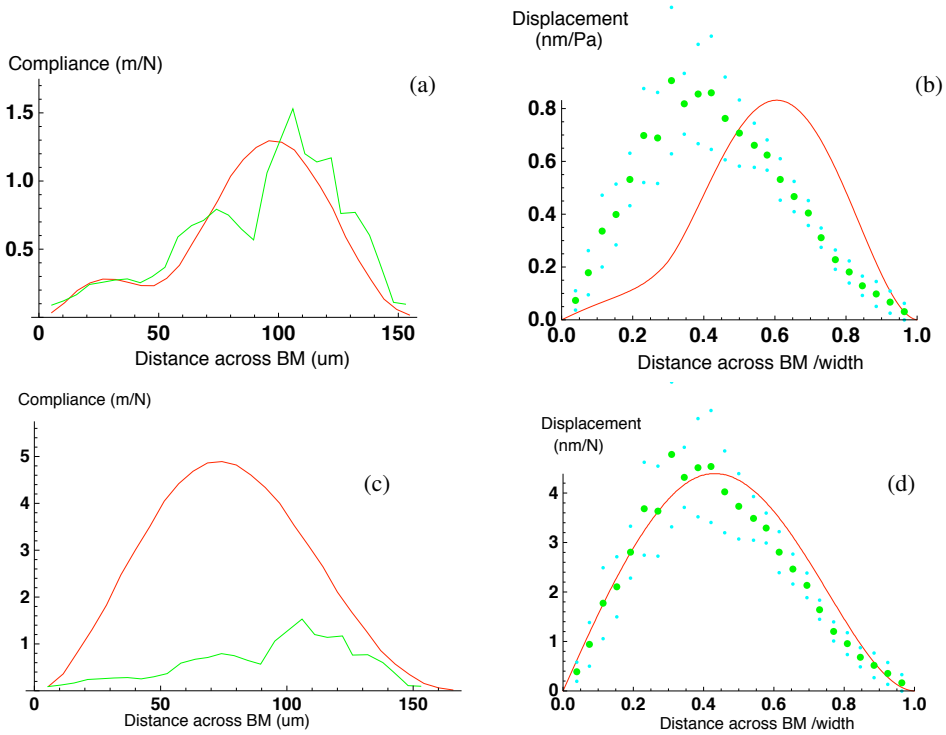


Figure 9. Beam model for fit with experimental measurements of BM in guinea pig. In (a) and (c) are the point load compliance results from specimen K1 by [Miller 1985] (green). In (b) and (d) is the BM displacement profile from [Cooper 2000] shown by the green dotted curve. The small green dots show the bounds. The calculations (red) are for the beam model with hinged support on the inner pillar and clamped support on spiral ligament. The thickness in AZ = 5 μm , thickness in PZ = 7.4 μm , width = 160 μm . The elastic properties are: $E_{AZ} = 0.09 \text{ GPa}$, $E_{PZ} = 0.021 \text{ GPa}$, outer pillar spring $k = 0.4 \text{ MPa}$. In (a) the model is fit to the point load measurements, (b) the same model displacement with pressure, showing a lack of fit with the Cooper profile. (c) Setting $k = 0$ in model yields a poor fit with measurements for the point loading, but (d) provides a reasonable agreement with Cooper for pressure loading.

Figure 9(a) shows the compliance at points across the basilar membrane as measured by a 10-micron probe in guinea pig K1 [Miller 1985]. Note the tendency for an increase in compliance at around 30 μm , which is in the AZ. It appears to be difficult to produce such behavior without a significant spring constant k corresponding to the OP. The result for the beam model (Figure 8) with the parameters chosen for a best fit is shown by the red curve in Figure 9(a). However, with the same elastic values, the response for pressure loading is compared to Cooper’s profile in Figure 9(b). A reasonable fit for both the point load and the pressure load for one beam model does not appear possible. The conclusion is that the effective spring constant k is not the same in the two loading cases. The consequence of keeping the beam properties the same, but setting $k = 0$, is a poor fit with the point load compliance (Figure 9(c)), but a good fit with Cooper’s profile in Figure 9(d).

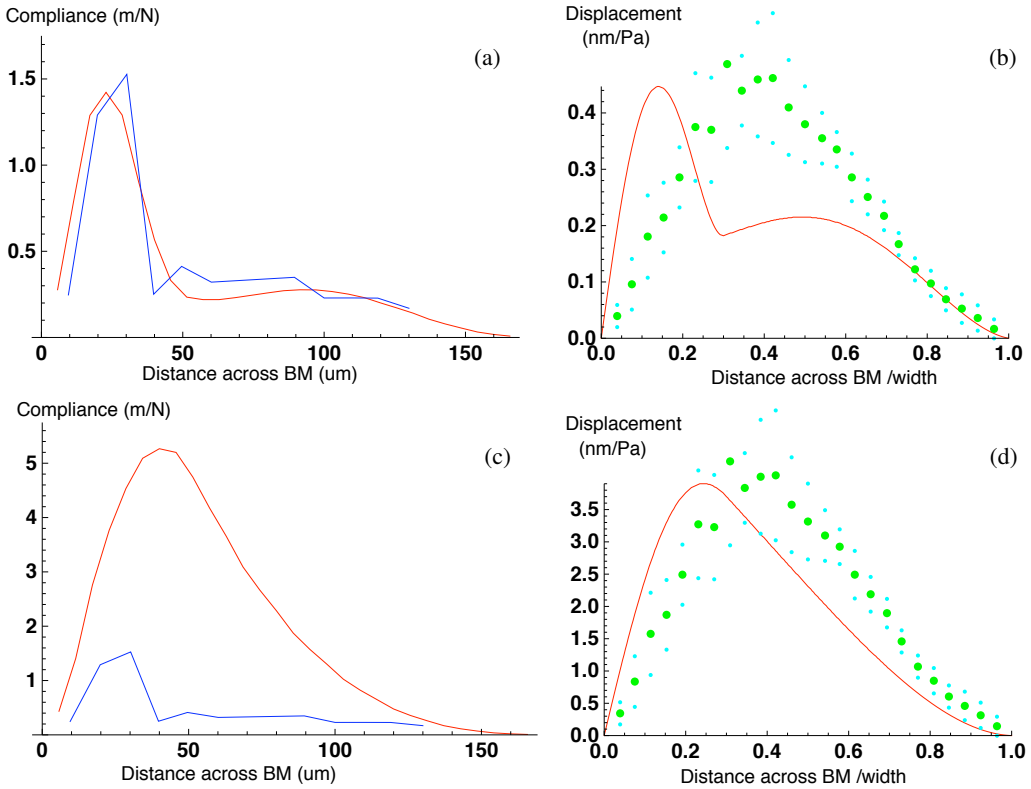


Figure 10. Beam model for fit with experimental measurements of BM in gerbil. In (a) and (c) are the point load compliance results in one gerbil by [Olson and Mountain 1994] (blue). In (b) and (d) is the BM displacement profile from [Cooper 2000] shown by the green dotted curve. The calculations (red) are for a solid beam model with hinged support on the inner pillar and clamped support on spiral ligament. The thickness in $AZ = 2.2 \mu\text{m}$, thickness in $PZ = 19 \mu\text{m}$, width = $160 \mu\text{m}$. The elastic properties are: $E_{AZ} = 0.09 \text{ GPa}$, $E_{PZ} = 0.011 \text{ GPa}$, outer pillar spring $k = 0.4 \text{ MPa}$. (a) The model is fit to point load measurements, (b) The same model displacement with pressure, showing a lack of fit with Cooper. (c) Setting $k = 0$ in model yields a poor fit for the point loading, but (d) a similarity to the Cooper profile for pressure loading.

The effect is more pronounced in gerbil. Figure 10(a) shows the compliance at points across the basilar membrane as measured in one gerbil by [Olson and Mountain 1994]. The red curve shows the beam model with parameters for a best fit. The response for pressure load is, however, quite unlike Cooper's profile, as shown in Figure 10(b). If the spring constant is set to zero ($k = 0$), the compliance under a point load is much too large (Figure 10(c)). However, the displacement under pressure is not far from Cooper's profile (Figure 10(d)). This is only a general indication, since in the gerbil BM the lower layer of collagen fibers are in the form of a large arc, rather than the flat plate in Figure 8.

The possible explanation for the inconsistency of the point and pressure loading lies in the orthotropic structure of the OC (Figures 2 and 3). Most elements are soft, such as the TM and the Hensen cells

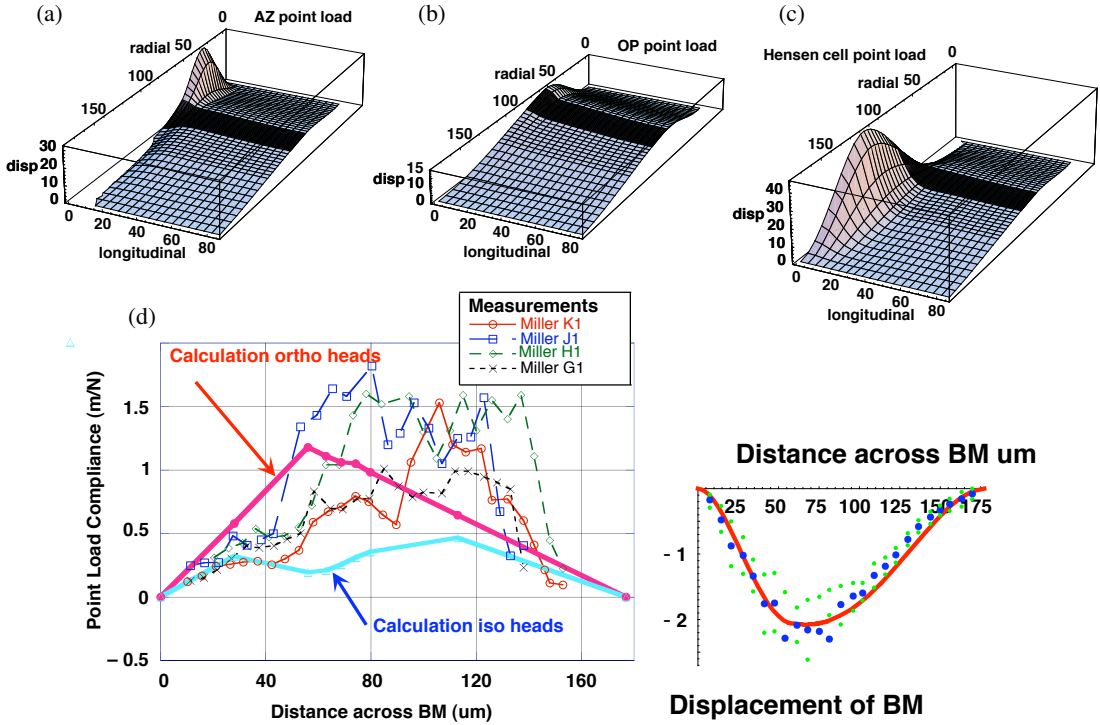


Figure 11. Fast4 full OC model with isotropic pillar heads for static pressure loading of the BM in the guinea pig base. Parts (a)–(c) show the displacement of a rectangular region of the BM consisting of the full width in the radial direction and 80 μm in the longitudinal direction, on one side of the 10 μm probe load. The displacement in the longitudinal direction decreases: (a) rapidly for load in the center of AZ, (b) slowly for load at the outer pillar, and (c) rapidly for load at the Hensen cells. (d) Magnitude of compliance under probe load from measurements and computation with isotropic and orthotropic heads. (e) Comparison with Cooper’s profile for pressure with isotropic heads.

on the right side, or discrete, such as the hair cells and the pillar cells. However, the heads of the pillars, just under the fluid region L1, consist of microtubules with high stiffness coupling in the direction perpendicular to the plane of Figures 2 and 3. Thus the array of pillars and heads will have an effective torsional stiffness. This could provide a significant stiffness k for the localized point load, but negligible effect for the pressure loading, when the neighboring pillars are moving together.

With the full model, Figures 2 and 3, the complete three-dimensional deformation due to a static point load can be computed as in Figure 11. So far as we are aware this is the first model calculation for this effect. The elastic and geometric properties are the same as in all the previous calculations, except for the longitudinal stiffness of the pillar heads. If the pillar head is isotropic, there is a substantial effect. Figure 11(a) shows the displacement of the BM when the point load is centered in the AZ. The decay of displacement in the radial direction is fairly gradual, due to the stiff radial fibers in the BM. In the longitudinal direction there are no fibers, only ground substance, and the decay is very rapid. For the load at the outer pillar, however, the pattern is quite different (Figure 11(b)). The total displacement

at the point load is smaller, and the decay in the longitudinal direction is much slower. This is clearly due to the torsional stiffness of the heads, that is, a resistance of one head from rotating with respect to its neighbors. Finally in Figure 11(c) the load is located at the Hensen cells in the PZ. For this, the displacement under the point load is large, and the decay in the longitudinal direction is rapid. Figure 11(d) shows the plot of the displacement under the point load for the load at different locations in the radial direction, as in Figure 9(a). Miller's measurements for four guinea pig cochleas are included. The continuous lines show the results from the calculations for the isotropic and orthotropic pillar heads. For the orthotropic values, that is, low torsional stiffness of the heads, the maximum displacement occurs for the load at the outer pillar. For the isotropic heads, however, the displacement for the load at the pillars has a minimum, giving a shape of the response similar to Miller's measurements. The amplitude is low by a factor of roughly 2, so a small modification of all the elastic properties is needed. Figure 11(e) shows the shape of the BM displacement under pressure compared with Cooper's profile with the isotropic heads. The tentative conclusion is that the full three-dimensional model (Figures 2 and 3) with isotropic pillar heads, unlike the simple beam model Figure 8 with fixed k , can explain both the point load measurements and the pressure deformation of the BM.

5. Dynamic response of organ of Corti

The next step is to consider the dynamic response of the OC for low frequency, for which in each fluid region the longitudinal motion of the fluid is negligible and the pressure is constant. Therefore the

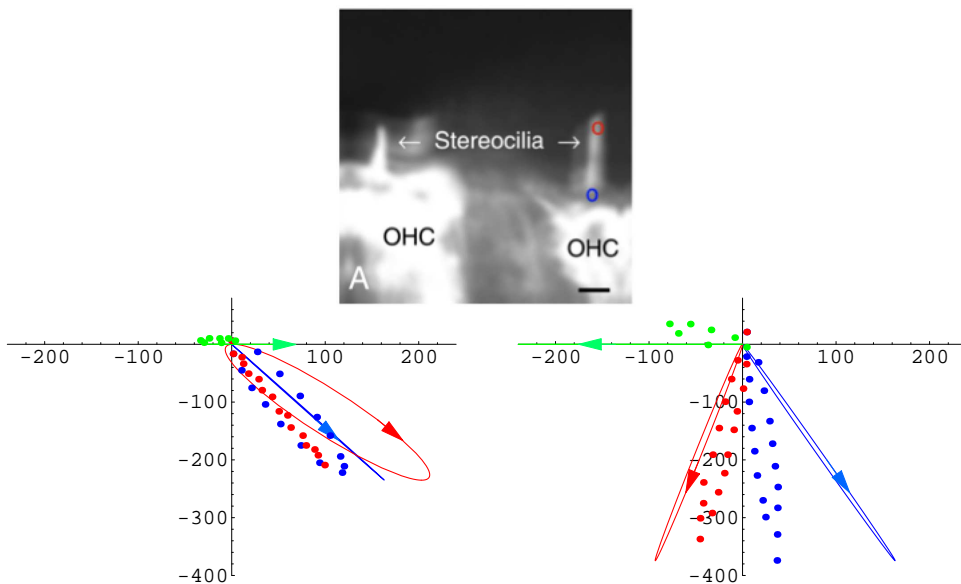


Figure 12. Displacement of tip and base of stereocilia at 200 Hz for around 85 dB SPL during one cycle of motion. Top: optical section. Bottom: dots show measurements [Fridberger et al. 2006] while curves show computed values. The horizontal and vertical axes show the displacement components tangent and perpendicular to the RL in nm. The curves are shifted so the maximum excursion during the cycle is the point at the origin.

problem is governed by Equation (6), containing only the elastic and viscous flow terms. Since no internal longitudinal flow occurs, the volume of fluid in the cross section is constant. The region of Cortilymph (C), surrounding the discrete OP and the OHC, is completely enclosed and so has no area change. Fluid flows between the regions IS, L1, L2, L3, and SV. This flow is governed by the permeability of viscous flow through and around the stereocilia. The pressures in the ducts SV and ST are prescribed to be equal in magnitude and opposite in sign. Thus the quantities in (6) are split into independent and dependent components [Steele and Puria 2005]. Following are new results.

5.1. Displacement of stereocilia. New capability is available for the optical imaging focused on the IHC and OHC stereocilia for motion at the frequency of 200 Hz [Fridberger et al. 2006]. Figure 12 (top) shows the image of the stereocilia of the IHC and OHC1. Details are obtained for the trajectory of the motion of the base and tip at 200 Hz. In Figure 12 (bottom) the measured values are shown by the dots and the Fast4 computation by the continuous lines. Of interest is that the tip motion is rather sensitive to the stiffness of TM and stereocilia, while the base motion is not. Note that the amplitude of displacement in Figure 12 (bottom) has a maximum of 400 nm, in comparison with the maximum amplitude of 12 μm for the static load steps in Figure 7. Measurements at lower sound intensity levels indicate that the response in Figure 12 is quite linear [Fridberger et al. 2006], so the buckling does not occur.

5.2. Phase of tip link tension. The linear solution of (6) with the IHC stereocilia and tip links included yields interesting results for the response for various initial gaps between the head of the tall stereocilium and the overlying TM and the adjacent HS [Steele and Puria 2005]. The phases of the different components for a soft TM and stiff OHC stereocilia at the guinea pig apex are shown in Figure 13. The

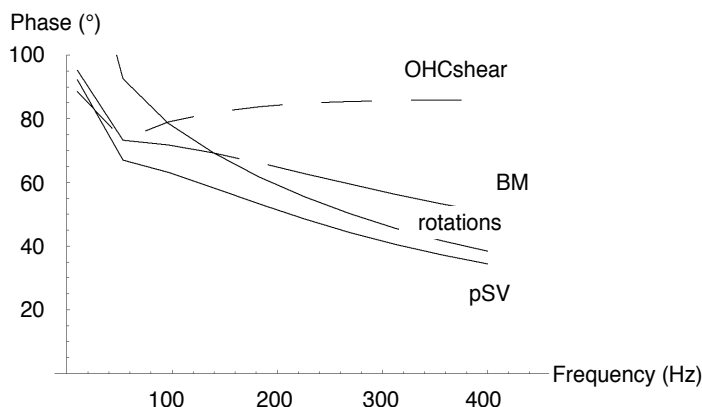


Figure 13. Phase of IHC tip link tension with respect to different components of the OC as computed from the model for the guinea pig apex for soft TM and stiff OHC stereocilia. The phases of the shear on the OHC, the BM displacement, the rotations of the stereocilia and the pressure in SV are not the same, as commonly assumed. The phase of tip link tension with respect to OHC shear is nearly 90° , similar to the measurements [Cheatham and Dallos 1999]. The phase difference between the relative rotation of the tall stereocilia of IHC and OHC1 is close to that measured [Fridberger et al. 2004].

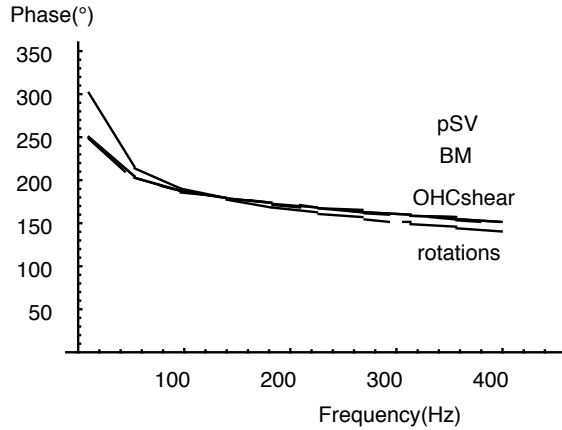


Figure 14. Phases for the guinea pig base calculated for OC with viscous fluid, with normal (*stiff*) TM and OHC stereocilia. Unlike the apex with the soft TM in Figure 13, the phase of the various quantities is essentially the same, as is usually assumed.

various quantities of OHC shear, BM displacement, pressure in SV, and relative rotation of IHC and OHC stereocilia, which are normally thought to be exactly in phase, are at somewhat different phases. At the base, however, with *stiff* TM and *stiff* OHC stereocilia, the phases of all the quantities are the same, as shown in Figure 14. The phase corresponds to excitation for displacement of the BM toward SV, qualitatively similar to the auditory nerve excitation reported [Ruggero et al. 2000]. However, this does not offer an explanation of the measurements [Fridberger et al. 2004], where a difference is found in BM displacement and electrical potential in the Cortilymph, similar to what we find in the apex in Figure 13, if the potential is related to the shear force on the OHC stereocilia.

To show that the phase depends on the stiffness of the overlying TM, the results for several orders of magnitude of the Young’s modulus are shown in Figure 15. The indication is [von Békésy 1960; Abnet and Freeman 2000] a value around 10–30 kPa, which gives the phase near 180°, that is, for excitation with BM displacement towards ST. The softer TM, accommodates to the fluid in L1 and the phase is

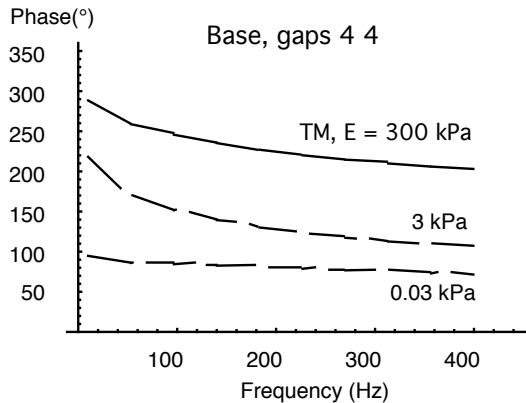


Figure 15. Dependency of phase of tip link tension on Young’s modulus of TM in the guinea pig base. This is the linear solution for initial gaps between the tall stereocilium tip and the TM and the HS both 4% of the tip radius.

case	cause	mechanism	effect on IHC neurons	phase
1	Small gap with HS (or high frequency). Tips of the tallest stereocilia of the IHC nearly stick to the HS.	Tip lags the base, causing decrease in tip link tension in phase with BM displacement.	inhibition	0°
2	Large gap with HS and TM (or lower frequency). Stereocilia are pulled through fluid.	Tip lags the base, causing decrease in tip link tension in phase with BM velocity.	inhibition	90°
3	Small gap with TM. Area of region L1 increases, and tips of the tallest stereocilia nearly stick to the TM, so L1 has negative pressure.	Outward pressure on stereocilium, causing increase in tip link tension in phase with BM displacement.	excitation	180°
4	Large gap with TM. The area of region L1 increases, so fluid flows from IS into L1.	Outward pressure on stereocilium, causing increase in tip link tension in phase with BM velocity.	excitation	270°

Table 1. Effects on phase of IHC tip link tension for BM motion toward ST, for which the base of the stereocilia moves in the positive radial direction. Cases 1 and 2 prevail for a relatively soft TM, while Cases 3 and 4 prevail for a relatively stiff TM.

near 90°, that is, for BM velocity toward SV. This range of TM modulus values seems extreme, but the lower value of 0.03 kPa may be near that for the bird TM, while the TM for the mustache bat is nearly pure collagen, with a modulus probably around 3 GPa.

Thus the phase can be anything, depending on the initial gaps and the stiffness. We attempt to sort out the main features in Table 1. Case 1 indicates the behavior if there is a small gap between the tip of the IHC stereocilium and the HS. For a thin fluid layer, high force is required to move the layers apart, so the tip of the stereocilium is nearly stuck to the HS. Displacement of the BM toward ST (downward in Figures 2 and 3) causes a bending of the stereocilium that reduces the tip link tension, which causes hyperpolarization of the cell and generally an inhibition of neural firing. If the gap is larger, Case 2, the stereocilium is pulled through the fluid which also reduces the tip link tension, but in phase with the BM velocity, which is a phase of 90° with respect to Case 1. Since the effect of the viscosity increases with frequency, there is a shift from Case 2 to Case 1 with increasing frequency, as seen in Figure 13 for the phase of tip link tension with respect to the BM displacement (curve labeled BM). This is generally the behavior expected with the phase somewhere between 0 and 90° [Cheatham and Dallos 1999]. The new feature [Steele and Puria 2005] is due to the geometry of the shell structure Figure 2, and 3, which shows the static deformation due to the pressure toward ST. Particularly note that the region L1 opens with this displacement of the BM. This behavior is confirmed by recent measurements in [Nowotny and Gummer 2006]. So this creates the possibility of Case 3 and Case 4 in Table 1 with phase of excitation of 180° and 270°. In Figure 14 for the guinea pig base the transition from Case 4 to Case 3 with increasing frequency is clear. In Figure 15 the transition from Cases 1–2 to Cases 3–4 with stiffening of the TM can be seen. For the soft TM, the opening of L1 has little effect, since the TM adapts to the fluid with minimum pressure.

5.3. Nonlinear response. For large displacements, buckling of the elastic structure is possible, as previously discussed. For acoustic excitation in the normal range, this does not seem to be significant. However, an obvious source of strong nonlinearity is the fluid gap between the tip of the IHC stereocilia and the HS and TM. In the previous work [Steele and Puria 2005] various results from lubrication theory are used, such as the formula for the force required to move a cylindrical surface with the radius R apart from a flat surface with the velocity \dot{g}_{HS}

$$F_{\text{fluid}} = -3\sqrt{2}\pi/\mu \dot{g}_{\text{HS}} \left(\frac{R}{g_{\text{HS}}} \right)^{3/2} \quad (7)$$

in which μ is the viscosity of the fluid and g_{HS} is the minimum distance between the two surfaces. For the linear solution, g_{HS} is fixed as the initial gap. For the nonlinear solution, however, g_{HS} is taken as the current gap. This nonlinearity affects only a few terms in the permeability matrix \mathbf{C} in (6). The nonlinear tenth-order system is solved using the forward integration function `NDSolve` in Mathematica. This requires around one minute for a given problem to compute several cycles of response.

The results for the force in the tip link of the IHC stereocilia for the guinea pig base at different intensities are in Figure 16. The input is a pressure difference between ST and SV, which varies sinusoidally, as shown by the blue curve in each plot. The positive maximum corresponds to maximum pressure toward SV, which causes shear on the OHC stereocilia in the excitatory direction. The solution is for the initial condition of zero displacement of all elements at time zero. It can be seen that what appears to be a nearly steady-state response is achieved in these few cycles. An expanded view for very small time shows that all displacements do start with zero as prescribed; there exist very short time response modes.

For low pressure, the response agrees closely with the linear steady-state solution. The maximum tension in the tip link for this frequency is nearly 180° out of phase with the pressure, that is, for pressure toward SV. For pressure of 30 Pa (corresponding to a sound pressure level, or SPL, of 124 dB), a small nonlinear effect appears as a distortion of the response curve consisting of a small plateau; see Figure 16(a). For a slight increase in pressure to 35 Pa (b), the plateau becomes a small secondary peak. For another step in pressure to 40 Pa (c), the secondary peak becomes positive. Thus there are two peaks of maximum tip link tension in each cycle. For another step to 50 Pa (d), the secondary peak becomes dominant. This secondary peak is almost in phase with the driving pressure. So, for a change in pressure corresponding to about 5 dB, there is a shift in the phase of the excitation of 180° . For a middle ear pressure gain from the ear canal to SV of 30 dB, this shift in phase would correspond to about 95 dB-SPL, close to the transition level reported [Ruggero et al. 2000]. What we do not see is the second shift back in phase occurring at about 30 dB higher pressure, as seen in the auditory nerve. The calculations show only an increase in the relative size of the secondary peak. Note that the out-of-phase peak stays about constant in (a–e), while the in-phase peak grows in amplitude. The theory uses resultant forces per unit length in the circumferential direction. However, this may be reduced to the effective force per tip link, which is the amplitude shown in Figure 16(a–d). These amplitudes appear to be consistent with the experiments on stereociliary bundles which yield the estimate that a Ca^{2+} -bound channel requires approximately 3 pN more force to open [Cheung and Corey 2006].

The change in the gap between the tip of the IHC tall stereocilium and the Hensen stripe is shown in Figure 16(f) for high pressure. The initial gap for these calculations is about 20 nm. So the gap is nearly

shut with the value of -20 nm, for almost half of the cycle in (f). Of course, the gap is never totally closed, since infinite force would be required.

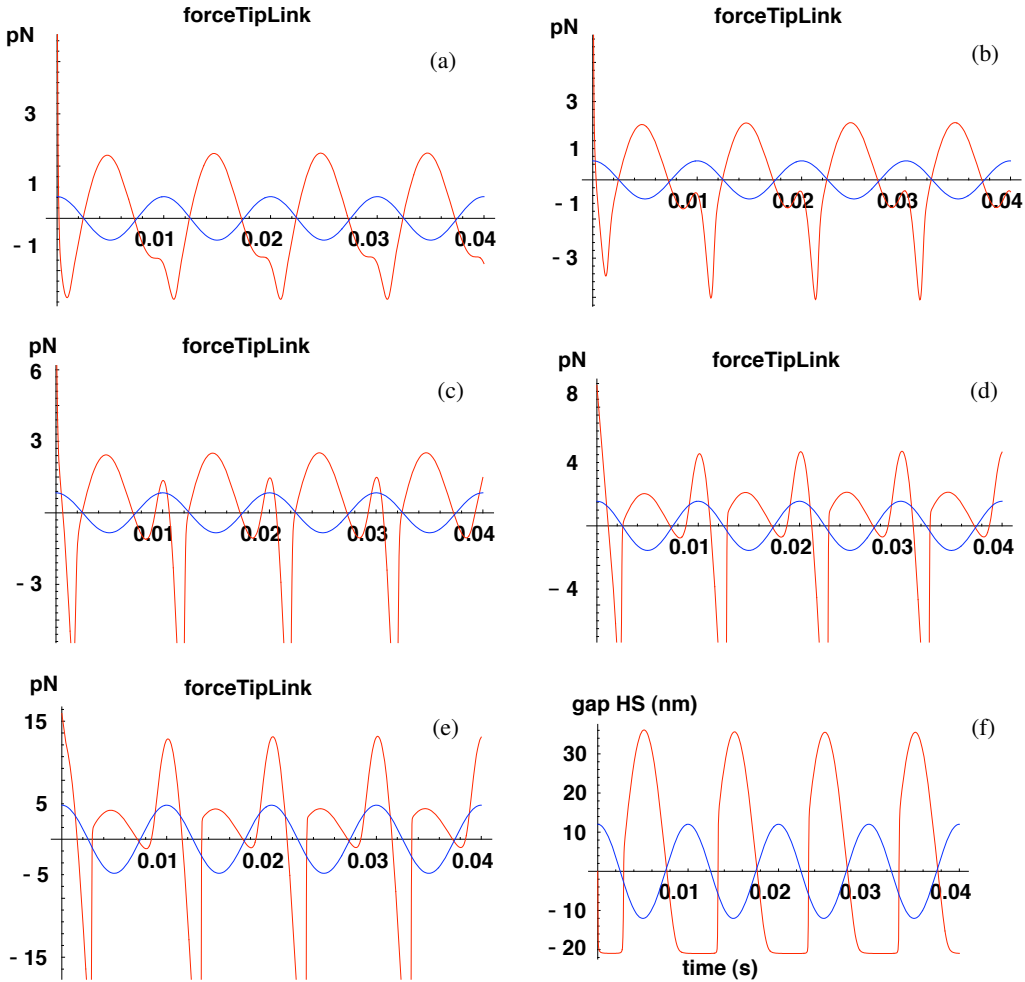


Figure 16. Nonlinear solution for the guinea pig base with initial gaps between the tip of IHC stereocilium and HS and TM of 7% (20 nm) at 100 Hz. (a) At the pressure difference ST-SV of 30 Pa the excitatory force in the tip link is out-of-phase with the pressure, but the negative portion acquires a secondary step that is in-phase. (b) At 35 Pa, the negative step becomes a small peak. (c) At 40 Pa, the secondary peak becomes positive. (d) At 50 Pa, the secondary peak becomes the dominant excitatory force. (e) At 60 Pa, the secondary peak becomes larger. (f) The gap between the Hensen stripe and the stereocilium tip shows that the secondary peak occurs when the tip comes into close contact. This offers an explanation for the 180° change in phase measured in auditory nerve fibers at 80 dB-SPL (in the ear canal) by [Ruggero et al. 2000]. Also the presence of the two excitatory peaks within the cycle (c)–(e) suggests a reason for the “peak splitting” sometimes observed in auditory nerve fibers.

6. Summary and discussion

The response of the organ of Corti shown in Figures 2–4 is a multidimensional problem, with the dimensions of the elastic elements ranging from millimeters to nanometers and the elastic moduli ranging from GPa to kPa. These components act together to transfer the input sound pressure into the proper neural excitation, so the separation of the process into uncoupled stages is not advantageous. All components are together in the shell-of-revolution simulation with the program Fast4. The recent advances in measurement are used to improve the elastic properties of components. With these one obtains the deformation shown in Figure 5 due to static pressure loading toward ST. This reveals a feature that is overlooked in simplified models. The subtektorial fluid region L1 opens in the vicinity of the inner hair cells. This opening of the fluid layer actually occurs, as shown by recent measurements in the guinea pig cochlea with electrical stimulation [Nowotny and Gummer 2006].

A good indication that the model components are put together properly comes from the superposition of the shell model and the optical image of the intact cross section [Fridberger et al. 2002], shown in Figure 4. The animation of the deformation due to steps in the static pressure load toward SV shows similar behavior of the model and actual organ of Corti. For loading in the opposite direction, [Fridberger et al. 2002] find a much larger response. The explanation is that a buckling of the outer pillars occurs, which can be seen in some of the images. This confirms that the IP and OP have an important role in maintaining the mechanical integrity of the OC. The optical signal does not have sufficient strength when passing deep into the tissue so the basilar membrane does not appear in the optical image.

The next paradox is the discrepancy between the measurements of the BM with point load and pressure. It seems that a simple beam model (Figure 8) cannot represent both. A possible explanation comes from the longitudinal stiffness of the pillar heads. This produces a significant torsional stiffness, which resists the deformation of the BM under a localized point load, but has much less effect for pressure. With isotropic pillar heads, in the three-dimensional model (Figures 2 and 3), both the point load and pressure conditions can be reasonably satisfied (Figure 11). The present analysis does not take into consideration the inclination of the hair cells and the phalangeal processes that connect the end of the hair cells to the RL. These will most likely provide additional longitudinal elastic coupling.

At this time the computational procedure for the full traveling wave solutions for all frequencies is not completed. However, there is interest in the low frequencies for which the longitudinal motion is not so significant, so the present three-dimensional model can be used. For these frequencies there is phase locking of the auditory nerve fibers. We assume that the neural excitation is proportional to the tension in the tip links (Figure 6). The results show excitation generally between BM displacement and velocity toward SV at the guinea pig apex. This is consistent with the intracellular recordings [Cheatham and Dallos 1999] and measurements of the relative rotation of IHC and OHC stereocilia [Fridberger et al. 2006] (Figure 12). At the guinea pig base, the phase of excitation is for BM motion toward ST, which is consistent with the direct measurements [Ruggero et al. 2000]. The key reason for this phase difference is that the fluid region under the TM and between the IHC and OHC stereocilia tends to open for BM motion toward ST. This causes fluid to flow in from the inner sulcus, bending the IHC stereocilia in the excitatory direction. In the apex, this is not so significant since the TM adapts more readily. The summary of the phase possibilities is in Table 1.

An important mechanical nonlinearity is caused by the small gap between the stereocilia of the IHC and the HS and TM. The actual initial gap will probably never be determined. Consequently in [Steele and Puria 2005], various values for this were assumed and some effect was found on the phase and amplitude of IHC excitation in the linear calculation of response. The present nonlinear calculation shows the effect of the amplitude of pressure on phase (Figure 16). For high pressure, corresponding to about 90 dB-SPL, the phase of the IHC excitation switches 180° . This is quite similar to the auditory nerve behavior sometimes observed [Ruggero et al. 2000]. Furthermore the intensity levels at which peak splitting develops, given in 1 dB steps in [Kiang 1990], look similar to the development of the two positive peaks in Figure 16. The negative peaks are most likely not realistic, since such sharp negative peaks are not seen in the IHC recordings [Cody and Mountain 1989]. This may be because the resting tension in the tip links is not included in these calculations. The neural behavior is variable [Cai and Geisler 1996], and the peak splitting and change in phase are not found in the guinea pig base [Wada et al. 2002]. However, it seems that the present calculations, based on the observation of the HS near the IHC stereocilia [Edge et al. 1998; Fridberger et al. 2006], support completely the notion that the Hensen stripe plays a crucial role in the excitation of the IHC. The suggestion is made [Zwislocki 1986] that there must be some mechanical nonlinear coupling between the TM and the OC. [Cody and Mountain 1989] provide further evidence for this. The present results appear to offer strong indication that the nonlinearity is simply due to the restricted fluid flow between the tip of the IHC stereocilia and the HS.

7. Conclusion

The cochlea of the inner ear offers significant challenges. The present consideration of passive static and low frequency response permits a focus on purely mechanical, that is, elastic-fluid aspects. The first task is the proper description of tissue components ranging over six orders of magnitude in size and elastic modulus. The assumption is that all of these behave elastically. Generally, we find consistency between the stiffness estimated from the microstructure and that computed from the available static measurements. The full three-dimensional shell model for the organ of Corti is necessary. This is evident from the consideration of the basilar membrane displacement under a point load and under pressure that cannot be described by a simple beam model.

The full model is certainly necessary to obtain the neural excitation, which is caused by fluid forces against the stereocilia of the inner hair cells. The full model shows effects missing from previous simplified models, in particular that a displacement of the basilar membrane causes an opening of the fluid region under the tectorial membrane. That opening and the proximity of the tips of the stereocilia to the Hensen stripe are critical for the phase of the excitation. Thus we offer an answer to long-standing questions on the phase of neural excitation. When the nonlinearity in the fluid layer is included, using lubrication theory, a change in the response is found with a small change in the amplitude of excitation, that offers an explanation for the long-standing question of neural peak splitting.

We have made some progress toward a satisfactory description of the tissue. An indication that all scales are represented properly is the agreement with experiments on the millimeter scale for BM point load response and on the nanometer scale for tip link forces. With this we have answered some basic questions. The challenge ahead is to obtain the high frequency response with the full model.

References

- [Abnet and Freeman 2000] C. C. Abnet and D. M. Freeman, “Deformations of the isolated mouse tectorial membrane produced by oscillatory forces”, *Hearing Res.* **144**:1–2 (2000), 29–46.
- [Andoh and Wada 2003] M. Andoh and H. Wada, “Dynamic characteristics of the force generated by the outer hair cell motility in the organ of Corti (theoretical consideration)”, *Trans. Jpn. Soc. Mech. Eng. C* **46**:4 (2003), 1256–1265.
- [von Békésy 1960] G. von Békésy, *Experiments in hearing*, edited by E. G. Wever, McGraw-Hill, New York, 1960.
- [Boutet 2007] J. Boutet de Monvel, M. Alessandro, J. Stefan, I. Tomo, M. von Tiedemann, A. Fridberger, M. Ulfendahl, and C. R. Steele, “From cochlear kinematics to cochlear mechanics: matching model to experiments”, *Otol. (Japan)* **17**:2 (2007), 76–84.
- [Cabezudo 1978] L. M. Cabezudo, “The ultrastructure of the basilar membrane in the cat”, *Acta Otolaryngol.* **86**:3 (1978), 160–175.
- [Cai and Chadwick 2002] H. Cai and R. Chadwick, “Radial structure of traveling waves in the inner ear”, *SIAM J. Appl. Math.* **63**:4 (2002), 1105–1120.
- [Cai and Geisler 1996] Y. Cai and C. D. Geisler, “Temporal patterns of the responses of auditory-nerve fibers to low-frequency tones”, *Hearing Res.* **96**:1–2 (1996), 83–93.
- [Carlini 1817] F. Carlini, “Ricerche sulla convergenza della serie che serve alla soluzione del problema di Keplero”, *Effem. Astron. (Milano)* **44**:1818 (1817), 3–48 (Appendice).
- [Cheatham and Dallos 1999] M. A. Cheatham and P. Dallos, “Response phase: a view from the inner hair cell”, *J. Acoust. Soc. Am.* **105**:2 (1999), 799–810.
- [Cheung and Corey 2006] E. L. M. Cheung and D. P. Corey, “Ca²⁺ changes the force sensitivity of the hair-cell transduction channel”, *Biophys. J.* **90**:1 (2006), 124–139.
- [Cody and Mountain 1989] A. R. Cody and D. C. Mountain, “Low-frequency responses of inner hair cells: evidence for a mechanical origin of peak splitting”, *Hearing Res.* **41**:2–3 (1989), 89–99.
- [Cooper 2000] N. P. Cooper, “Radial variation in the vibrations of the cochlear partition”, pp. 109–115 in *Proceedings of the International Symposium on Recent Developments in Auditory Mechanics* (Sendai, 1999), edited by H. Wada et al., World Scientific, Singapore, 2000.
- [Edge et al. 1998] R. M. Edge, B. N. Evans, M. Pearce, C.-P. Richter, X. Hu, and P. Dallos, “Morphology of the unfixed cochlea”, *Hearing Res.* **124**:1–2 (1998), 1–16.
- [Freeman et al. 2003] D. M. Freeman, C. C. Abnet, W. Hemmert, B. S. Tsai, and T. F. Weiss, “Dynamic material properties of the tectorial membrane: a summary”, *Hearing Res.* **180**:1–2 (2003), 1–10.
- [Fridberger et al. 2002] A. Fridberger, J. Boutet de Monvel, and M. Ulfendahl, “Internal shearing within the hearing organ evoked by basilar membrane motion”, *J. Neurosci.* **22**:22 (2002), 9850–9857.
- [Fridberger et al. 2004] A. Fridberger, J. Boutet de Monvel, J. Zheng, N. Hu, Y. Zou, T. Ren, and A. Nuttall, “Organ of Corti potentials and the motion of the basilar membrane”, *J. Neurosci.* **24**:45 (2004), 10057–10063.
- [Fridberger et al. 2006] A. Fridberger, I. Tomo, M. Ulfendahl, and J. Boutet de Monvel, “Imaging hair cell transduction at the speed of sound: dynamic behavior of mammalian stereocilia”, *Proc. Nat. Acad. Sci. U.S.A.* **103**:6 (2006), 1918–1923.
- [Geisler 1998] C. D. Geisler, *From sound to synapse: physiology of the mammalian ear*, Oxford University Press, New York, 1998.
- [Givelberg and Bunn 2003] E. Givelberg and J. Bunn, “A comprehensive three-dimensional model of the cochlea”, *J. Comput. Phys.* **191**:2 (2003), 377–391.
- [Gray 1918] H. Gray (revised by W. H. Lewis), *Anatomy of the human body*, 20th ed., Lea & Febiger, Philadelphia, 1918. Reproduced in <http://www.bartleby.com/107>.
- [Helle 1974] R. Helle, *Beobachtungen an hydromechanischen Modellen des Innenohres mit Nachbildung von Basilmembran, Corti-Organ und Deckmembran*, Ph.D. Thesis, Technical University of Munich, 1974.
- [Homer et al. 2004] M. Homer, A. Champneys, G. Hunt, and N. P. Cooper, “Mathematical modeling of the radial profile of basilar membrane vibrations in the inner ear”, *J. Acoust. Soc. Am.* **116**:2 (2004), 1025–1034.

- [Kelly 1989] J. P. Kelly, “Cellular organization of the guinea pig’s cochlea”, *Acta Otolaryngol. Suppl.* 467 (1989), 97–112.
- [Kiang 1990] N. Y. Kiang, “Curious oddments of auditory-nerve studies”, *Hearing Res.* **49**:1–3 (1990), 1–16.
- [Langer et al. 2001] M. G. Langer, S. Fink, A. Koitschev, U. Rexhausen, J. K. H. Hörber, and J. P. Ruppertsberg, “Lateral mechanical coupling of stereocilia in cochlear hair bundles”, *Biophys. J.* **80**:6 (2001), 2608–2621.
- [Miller 1985] C. E. Miller, “Structural implications of basilar membrane compliance measurements”, *J. Acoust. Soc. Am.* **77**:4 (1985), 1465–1474.
- [Narayan et al. 1998] S. S. Narayan, A. N. Temchin, A. Recio, and M. A. Ruggero, “Frequency tuning of basilar membrane and auditory nerve fibers in the same cochleae”, *Science* **282**:5395 (1998), 1882–1884.
- [Nowotny and Gummer 2006] M. Nowotny and A. W. Gummer, “Nanomechanics of the subtectorial space caused by electromechanics of cochlear outer hair cells”, *Proc. Nat. Acad. Sci. U.S.A.* **103**:7 (2006), 2120–2125.
- [Olson 1998] E. S. Olson, “Observing middle and inner ear mechanics with novel intracochlear pressure sensors”, *J. Acoust. Soc. Am.* **103**:6 (1998), 3445–3463.
- [Olson and Mountain 1994] E. S. Olson and D. C. Mountain, “Mapping the cochlear partition’s stiffness to its cellular architecture”, *J. Acoust. Soc. Am.* **95**:1 (1994), 395–400.
- [Olver 1974] F. J. W. Olver, *Asymptotics and special functions*, Academic Press, New York, 1974.
- [Ranke 1950] O. F. Ranke, “Theory of operation of the cochlea: a contribution to the hydrodynamics of the cochlea”, *J. Acoust. Soc. Am.* **22**:6 (1950), 772–777.
- [Ruggero et al. 2000] M. A. Ruggero, S. S. Narayan, A. N. Temchin, and A. Recio, “Mechanical bases of frequency tuning and neural excitation at the base of the cochlea: comparison of basilar-membrane vibrations and auditory-nerve-fiber responses in chinchilla”, *Proc. Nat. Acad. Sci. U.S.A.* **97**:22 (2000), 11744–11750.
- [Scherer and Gummer 2004] M. P. Scherer and A. W. Gummer, “Impedance analysis of the organ of Corti with magnetically actuated probes”, *Biophys. J.* **87**:2 (2004), 1378–1391.
- [Shoelson et al. 2004] B. Shoelson, E. K. Dimitriadis, H. Cai, B. Kachar, and R. S. Chadwick, “Evidence and implications of inhomogeneity in tectorial membrane elasticity”, *Biophys. J.* **87**:4 (2004), 2768–2777.
- [Spector et al. 1999] A. A. Spector, W. E. Brownell, and A. S. Popel, “Mechanical and electromotile characteristics of auditory outer hair cells”, *Med. Biol. Eng. Comput.* **37**:1 (1999), 247–251.
- [Steele 1999] C. R. Steele, “Toward three-dimensional analysis of cochlear structure”, *ORL J. Oto-Rhino-Lary.* **61**:5 (1999), 238–251.
- [Steele and Puria 2005] C. R. Steele and S. Puria, “Force on inner hair cell cilia”, *Int. J. Solids Struct.* **42**:21–22 (2005), 5887–5904.
- [Steele and Shad 1995] C. R. Steele and K. u.-R. Shad, “Asymptotic-numeric solution for shells of revolution”, *Appl. Mech. Rev. (ASME)* **48**:11, part 2 (1995), S44.
- [Steele and Taber 1979] C. R. Steele and L. A. Taber, “Comparison of WKB calculations and experimental results for three-dimensional cochlear models”, *J. Acoust. Soc. Am.* **65**:4 (1979), 1007–1018.
- [Steele et al. 2005] C. R. Steele, M. P. Scherer, C. Chandrasekaran, and A. W. Gummer, “An analytic model for the mechanical point impedance of the organ of Corti”, poster session of the 28th annual midwinter research meeting of the Association for Research in Otolaryngology, 2005.
- [Tolomeo and Holley 1997] J. A. Tolomeo and M. C. Holley, “Mechanics of microtubule bundles in pillar cells from the inner ear”, *Biophys. J.* **73**:4 (1997), 2241–2247.
- [Wada et al. 2002] H. Wada, A. Takeda, and T. Kawase, “Timing of neural excitation in relation to basilar membrane motion in the basal region of the guinea pig cochlea during the presentation of low-frequency acoustic stimulation”, *Hearing Res.* **165**:1–2 (2002), 165–176.
- [Wikipedia 2004] Illustration in Wikipedia entries relating to the inner ear, 2004, Available at <http://commons.wikimedia.org/wiki/File:Cochlea-crosssection.png>. Attributed to Oarih Ropschkow.
- [Wittbrodt et al. 2006] M. J. Wittbrodt, C. R. Steele, and S. Puria, “Developing a physical model of the human cochlea using microfabrication methods”, *Audiol. Neurotol.* **11**:2 (2006), 104–112.

[Yoon et al. 2006] Y.-J. Yoon, S. Puria, and C. R. Steele, “Intracochlear pressure and organ of Corti impedance from a linear active three-dimensional model”, *ORL J. Oto-Rhino-Lary.* **68**:6 (2006), 365–372.

[Zetes et al. 2004] D. E. Zetes, J. A. Tolomeo, and M. C. Holley, “Mapping the mechanical properties of cytoskeletal structures in the mammalian inner ear”, 2004. Manuscript.

[Zwislocki 1986] J. J. Zwislocki, “Are nonlinearities observed in firing rates of auditory-nerve afferents reflections of a nonlinear coupling between the tectorial membrane and the organ of Corti?”, *Hearing Res.* **22**:1–3 (1986), 217–221.

Received 8 Dec 2008. Accepted 26 Jan 2009.

CHARLES R. STEELE: chasst@stanford.edu

Stanford University, Mechanical Engineering, Durand Building, Room 262, Stanford, CA 94305-4035, United States

JACQUES BOUTET DE MONVEL: jmonvel@pasteur.fr

Unité de Génétique et Physiologie de L’Audition, Inserm UMRS 587, Institut Pasteur, 25 Rue du Dr. Roux, 75724 Paris, cedex 15, France

SUNIL PURIA: puria@stanford.edu

Stanford University, Mechanical Engineering, Durand Building, Room 262, Stanford, CA, 94305-4035, United States

and

Stanford University, Otolaryngology — Head and Neck Surgery, Stanford, CA 94305, United States